

Towards Unified Structured Light Optimization

Tinglei Wan
Harbin Institute of Technology

Tonghua Su
Harbin Institute of Technology

Zhongjie Wang
Harbin Institute of Technology

Abstract

Structured light (SL) 3D reconstruction captures the precise surface shape of objects, providing high-accuracy 3D data essential for industrial inspection and robotic vision systems. However, current research on optimizing projection patterns in SL 3D reconstruction faces two main limitations: each scene requires separate training of calibration parameters, and optimization is restricted to specific types of SL, which restricts their application range. To tackle these limitations, we present a unified framework for SL optimization, adaptable to diverse lighting conditions, object types, and different types of SL. Our framework quickly determines the optimal projection pattern using only a single projected image. Key contributions include a novel global matching method for projectors, enabling precise projector-camera alignment with just one projected image, and a new projection compensation model with a photometric adjustment module to reduce artifacts from out-of-gamut clipping. Experimental results show our method achieves superior decoding accuracy across various objects, SL patterns, and lighting conditions, significantly outperforming previous methods.

1. Introduction

Structured light (SL) 3D reconstruction has significant applications in several critical fields due to its non-contact nature and high precision. In robotics, SL systems are used for pose estimation [5, 30, 32] and precise positioning [14, 31, 35, 37]. In biological sciences, SL 3D reconstruction can accurately capture the 3D shapes of plant [2, 18, 29, 38] and animal skeletons [3, 4, 20, 22, 25], which is essential for creating digital biological databases. In industrial inspection, SL 3D reconstruction technology facilitates rapid reverse engineering [1, 26] and online quality control [27, 33].

Some research has been conducted on optimizing the

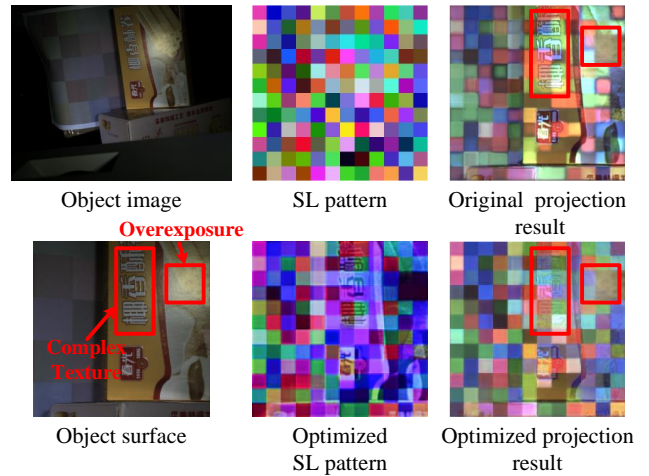


Figure 1. Challenging lighting environment and the texture of the object’s surface can cause errors in the SL encoding information. The algorithm we propose can effectively reduce such errors.

projection side of SL 3D reconstruction, particularly in designing illumination coding strategies; however, current efforts have not considered adaptive projection pattern optimization for challenging lighting conditions and complex object textures, as shown in Fig. 1. While most research has focused on post-processing measurement data captured by cameras—such as noise removal, plane refocusing, and compensating for phase shift errors—there has been little attention to optimizing projection patterns based on the principles of image formation. SL 3D reconstruction methods are inherently proactive, especially in manipulating illumination, but existing approaches often rely on heuristic methods like composite coding, frequency multiplexing, and color multiplexing. These methods, however, are not learnable and do not guarantee the optimal recovery of the necessary information.

Projection compensation techniques enable modeling of the projection process, making it possible to adaptively ad-

just projection patterns according to environmental lighting and object textures, thus offering potential for optimizing SL patterns [21, 34, 36]. However, these techniques face significant challenges that limit their direct application. While these techniques can correct color deviations caused by ambient light and complex projection surfaces [8, 17, 19], two major issues arise. First, accurately mapping surface reflection information from the object to the projector image plane is complex. This limits the techniques to simple surfaces, such as flat or singly curved ones, which are less representative of the complex geometries encountered in 3D reconstruction. Second, projection compensation functions are scene-specific, requiring a large number of patterns to be projected for each scene to train photometric parameters, making them impractical for direct application.

To address these challenges, we propose a unified optimization framework for SL (Fig. 2), which only requires a single projection to calibrate photometric properties and optimize the SL pattern through compensation. Our approach introduces a global matching method that projects a single image onto the object surface to locate key points. Using 2D planar triangulation texture mapping, we achieve global and continuous matching, enabling rapid alignment of the projector image plane with any object surface. Additionally, a projection compensation network is constructed by integrating surface reflection information under ambient light. We refine this network using a TPS color mapping function and constraints from the projector alignment images, ensuring effective compensation for any input.

Our contributions can be summarized as follows:

- We propose a novel unified framework for adaptive SL. This framework enables rapid photometric calibration with a single projection and optimizes any type of SL pattern through projection compensation, adapting to various objects and environments.
- We propose a global matching technique that requires only a single projection, offering faster performance than other projector-camera matching methods and achieving continuous mapping with sub-pixel accuracy.
- We propose a SL projection compensation model. It reduces artifacts from traditional compensation models during pattern optimization and ultimately improves decoding accuracy in SL 3D reconstruction.

2. Related Work

Our proposed unified framework for SL optimization consists of two main components: projector-camera global matching and projection compensation. We first introduce related work in these two areas. Additionally, we introduce various recent attempts by researchers to generate SL patterns that are better adapted to the capturing scene.

2.1. Projector-Camera Global Matching

Projector-camera global matching methods can be broadly categorized based on the continuity of the projection surface. For continuous surfaces, Raskar et al. [28] proposed using a 3x3 single-response matrix for pixel correspondence, suitable only for ideal planar surfaces. Huang et al. [11] extended this to curved surfaces by constructing a warping network based on Thin-Plate Splines (TPS) and affine transformations, but this approach requires extensive training data for each specific scene, limiting its practicality in varied environments. For non-continuous surfaces, Gupta et al. [9] designed a composite Gray code pattern for matching, while Pages et al. [23] used sinusoidal SL patterns to calculate the phase of each pixel, requiring multiple projections. These methods, though accurate, are time-consuming and inefficient for real-time applications. Specialized equipment can expedite the matching process. Fujii et al. [8] used a coaxial optical system to avoid parallax, and Park et al. [24] employed an RGBD camera with grid images, achieving matching through online optimization with differentiable rendering. However, these approaches depend on specialized equipment, which may not be available or feasible in all scenarios.

2.2. Projector Compensation

Projector compensation methods can be broadly divided into traditional non-deep learning approaches and more recent deep learning approaches. Traditional methods achieve compensation by modifying the projector’s input to account for the photometric environment. For instance, Raskar et al. [28] established a mapping between the projector input and output, calculating a compensation function in color space. However, these methods struggle with complex optical interactions on surfaces with arbitrary geometries and colors and typically rely on gray code patterns, resulting in a discrete mapping unsuitable for complex surfaces. Deep learning approaches have shown superior results. Huang et al. [12] introduced a model that separates projection information from non-projected surfaces, while Park et al. [24] used a virtual rendering process to optimize the input image, reducing visual artifacts. However, these methods also have limitations. Huang’s approach requires extensive data retraining for different surfaces, and Park’s method, while avoiding retraining, introduces additional equipment requirements and potential calibration errors. Both approaches often require retraining for new environments, limiting their direct application in optimizing projection inputs for SL-based 3D reconstruction.

2.3. Structural Light Projection Optimization

Recently, there have been several studies on the optimization of SL projection patterns. Xu et al. [39] composed SL encoding using an LED array and LCD mask, obtaining

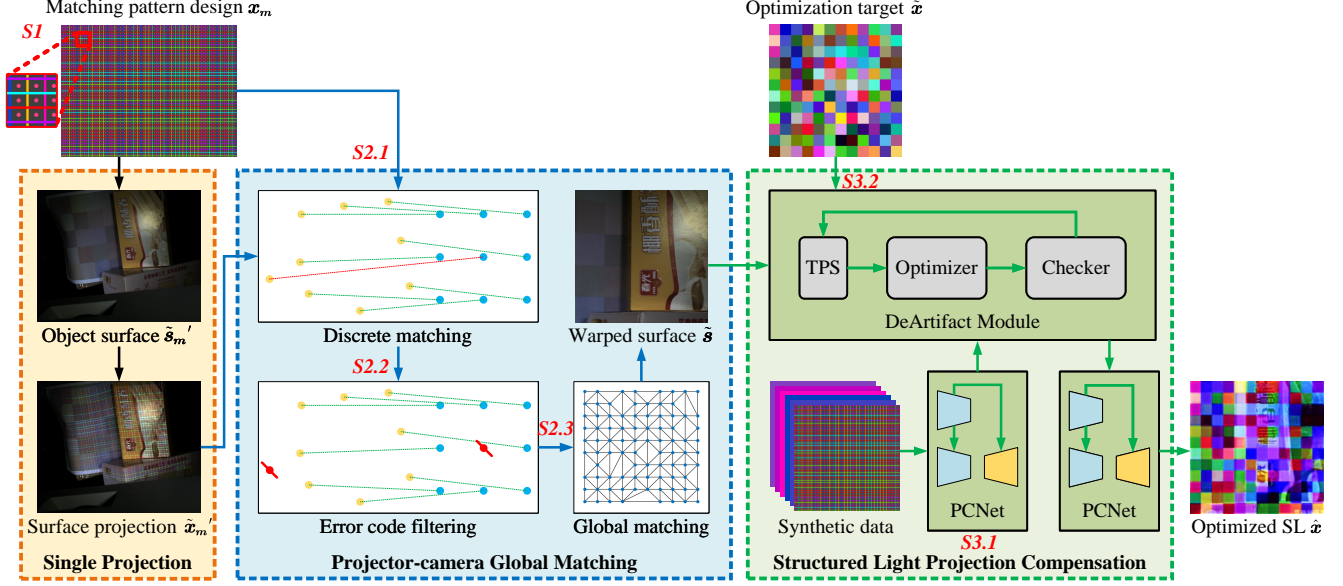


Figure 2. Unified structured light projection optimization framework.

the optimal SL encoding for the environment by learning multiple sets of optimal mask patterns, and subsequently aggregating decoded results from multiple LEDs captured by the camera to generate the final depth map. Dong et al. [6] proposed an adaptive method for color SL in ambient light, first quickly identifying the most distinct colors that are easily separable under new environmental and device settings, then utilizing a maximum a posteriori (MAP) based color detection method to robustly detect SL colors. Jia et al. [13] proposed depth-adaptive speckle SL, representing speckle by three parameters: gray level, density, and size, then uniformly dividing the projected pattern into several sub-regions, and regressing the speckle parameters of each sub-region based on prior depth to ensure even illumination of the object surface. The optimization schemes for SL projection patterns mentioned above have achieved good results for their specific projection inputs. However, they are limited to optimizing specific types of SL; for instance, Xu’s method cannot optimize color SL, Dong’s method is unsuitable for grayscale SL, and Jia’s method is restricted to speckle SL. Consequently, these methods struggle to be generalized to more diverse scenes.

3. Methodology

In this section, we introduce the details of our unified adaptive SL projection optimization framework. As shown in Fig. 2, the overall system architecture is composed of two key components: projector-camera global matching and SL projection compensation. The projector-camera global matching method achieves continuous global matching by

Algorithm 1 Optimizing Structured Light Pattern

- 1: **Input:** \tilde{x} : Optimization target
- 2: **Output:** \hat{x} : Optimized SL pattern
- 3: **Initialize:** $P = \emptyset, C = \emptyset, A_{hor} = \{1, 3, 5, 7\}, A_{ver} = \{2, 4, 6, 8\}, \mathbf{v} = (0.25, 0.25, 0.25)$
- 4: // Stage 1: Generate Matching Pattern
- 5: $\mathbf{x}_m = \mathbf{GeneratePattern}(A_{hor}, A_{ver}, \mathbf{v})$
- 6: $\tilde{\mathbf{x}}_m' = \mathbf{Project}(\tilde{\mathbf{s}}_m', \mathbf{x}_m)$
- 7: // Stage 2: Projector-Camera Global Matching
- 8: // Stage 2.1: Discrete Matching
- 9: $P, C = \mathbf{FindFeaturePoint}(\mathbf{x}_m, \tilde{\mathbf{x}}_m')$
- 10: $M = \mathbf{DeBruijnDecode}(P, C)$
- 11: // Stage 2.2: Error Code Filtering
- 12: $(X_{map}^p, Y_{map}^p) = \mathbf{PositionMap}(P)$
- 13: $(X_{map}^c, Y_{map}^c) = \mathbf{PositionMap}(C)$
- 14: $S_x, S_y = \mathbf{ErrorVote}(X_{map}^p, Y_{map}^p, X_{map}^c, Y_{map}^c)$
- 15: $M \leftarrow \mathbf{ErrorFilter}(M, S_x, S_y)$
- 16: // Stage 2.3: Global Matching
- 17: $T = \mathbf{Triangulate}(M)$
- 18: $\tilde{\mathbf{s}} = \mathbf{GlobalMatch}(\tilde{\mathbf{s}}_m', T)$
- 19: // Stage 3: SL Projection Compensation
- 20: // Stage 3.1: Compensation Process Modeling
- 21: $PCNet = \mathbf{NetworkTrain}(\tilde{\mathbf{x}}; \mathbf{x}; \tilde{\mathbf{s}})$
- 22: // Stage 3.2: De-artifacting
- 23: $\text{SyntheticDatas} = \{\mathbf{x}_m, \tilde{\mathbf{x}}_m', PCNet(\text{SolidColor})\}$
- 24: $TPS = \mathbf{Optimizer}(\text{SyntheticDatas})$
- 25: $\text{Mask} = \mathbf{Checker}(TPS, \text{SyntheticDatas})$
- 26: $\hat{\mathbf{x}} = PCNet(\text{Mask}(TPS(\tilde{\mathbf{x}})), \tilde{\mathbf{x}})$

triangulating feature points, effectively converting discrete matching points into a continuous matching surface. This approach provides robustness against incorrect matches. Meanwhile, the SL projection compensation method introduces a novel compensation framework that effectively reduces the impact of artifacts. The overall algorithm pseudocode of the framework is shown in Alg. 1.

3.1. Projector-camera Global Matching

3.1.1. Matching Pattern Design

To optimize the SL pattern, it is essential to determine the position of each pixel as it is projected onto the object and captured by the camera. We designed SL images using De Bruijn [15] sequences for this purpose. In our method, the horizontal alphabet $A_{hor} = \{1, 3, 5, 7\}$ corresponds to red, lime, cyan, and purple, while the vertical alphabet $A_{ver} = \{2, 4, 6, 8\}$ represents yellow, green, blue, and magenta. With a window length of 3, no sequence of three consecutive lines repeats, allowing unique identification of stripe intersections. To increase the number of matching feature points, orange-red dots are placed at the center of the grid.

To provide more reference data for projection compensation, we set the background color of the pattern within the range (0.25, 0.25, 0.25) to (0.75, 0.75, 0.75). The Euclidean distance between three vectors representing (R, G, B) was used to calculate the maximum separation from the grid colors in color space, ensuring that the background does not interfere with stripe detection or cause brightness clipping. The optimal background color identified was $\mathbf{v} = (0.25, 0.25, 0.25)$.

3.1.2. Discrete Matching and Error Code Filtering

Project the pattern shown in Fig. 2 onto the object and use De Bruijn coding to match feature points. This results in discrete sets of projector-camera matching points, $P = \{p_i = (x_p^i, y_p^i), i = 1, 2, \dots, n\}$ and $C = \{c_i = (x_c^i, y_c^i), i = 1, 2, \dots, n\}$. The matching relationship between these points can be described as a bijection $M = \{(p_i, c_i) | p_i \in P, c_i \in C, i=1,2,\dots,n\}$ from the projector points P to the camera points C .

During the matching process, De Bruijn code losses in some regions can lead to decoding errors in the grid's central feature points. This requires detecting and removing these errors to prevent error codes from being carried into the subsequent global matching process.

We compute the horizontal and vertical relative position matrices, X_{map}^p and Y_{map}^p on the projector image plane, and X_{map}^c and Y_{map}^c on the camera image plane, by comparing the relative positions of the feature points (x_p^i, y_p^i) and (x_c^i, y_c^i) with their surrounding eight feature points. Eq. 1 presents the XOR of these matrices, indicating the similar-

ity between the two sets of position encodings.

$$V_x = X_{map}^p \oplus X_{map}^c, \quad V_y = Y_{map}^p \oplus Y_{map}^c. \quad (1)$$

Finally, by performing row summation on V_x and V_y , we can obtain the voting scores for error codes in the x and y analyses, S_x and S_y , for each point. Let the elements in S_x and S_y be S_x^i and S_y^i , respectively. The indices of the points to be filtered out are determined as Eq 2.

$$\text{indices} = \{i \mid i \in \{1, 2, \dots, n\} \text{ and } (S_x^i \geq k \text{ or } S_y^i \geq k)\}. \quad (2)$$

The value of k is related to the number of points n involved in the error code check. Generally, k is set as $\text{Floor}(n/2)$, where $\text{Floor}(\cdot)$ denotes the floor function.

3.1.3. Global Matching

To achieve continuous global mapping, we introduce the use of Delaunay triangulation to convert discrete matches into continuous mappings for the first time. This extends M to every pixel on the projector image plane by triangulating the point set P , forming a continuous triangular mesh where each vertex p_1, p_2, p_3 corresponds to camera image coordinates c_1, c_2, c_3 .

For any point $p = (x_p, y_p)$ within a triangular patch, its barycentric coordinates calculated using Eq. 3 to 6.

$$\det T = (y_p^2 - y_p^3)(x_p^1 - x_p^3) + (x_p^3 - x_p^2)(y_p^1 - y_p^3), \quad (3)$$

$$L_1 = \frac{(y_p^2 - y_p^3)(x_p - x_p^3) + (x_p^3 - x_p^2)(y_p - y_p^3)}{\det T}, \quad (4)$$

$$L_2 = \frac{(y_p^3 - y_p^1)(x_p - x_p^3) + (x_p^1 - x_p^3)(y_p - y_p^3)}{\det T}, \quad (5)$$

$$L_3 = 1 - L_1 - L_2. \quad (6)$$

If p lies within the triangle formed by p_1, p_2, p_3 , then $L_1 \geq 0, L_2 \geq 0$, and $L_3 \geq 0$. The corresponding texture coordinates $c(x_c, y_c)$ can be obtained through barycentric interpolation.

$$\begin{cases} x_c = L_1 \cdot x_c^1 + L_2 \cdot x_c^2 + L_3 \cdot x_c^3 \\ y_c = L_1 \cdot y_c^1 + L_2 \cdot y_c^2 + L_3 \cdot y_c^3 \end{cases}. \quad (7)$$

By traversing each triangular patch on the projector image plane and performing barycentric interpolation for the points inside, corresponding camera coordinates are calculated, establishing a continuous global mapping between the projector and the camera.

3.2. Structured Light Projection Compensation

3.2.1. Compensation Process Modeling

To achieve adaptive adjustment of the projection input based on lighting and object reflectance, we need to model the projection process, which is represented by Eq. 8.

$$\mathbf{x}^* = \mathcal{F}^\dagger(\mathbf{x}; \tilde{\mathbf{s}}), \quad (8)$$

where \tilde{s} is the surface image of the object under global illumination, \mathbf{x}^* is the SL projection pattern, and \mathbf{x} is the projection pattern captured by the camera. To ensure that the projection pattern is unaffected by ambient light or object surface texture, we set the initial pattern as \mathbf{x}_0 and the ideal captured image as $\mathbf{x} = \mathbf{x}_0$. The optimized projection pattern is obtained using:

$$\hat{\mathbf{x}} = \mathcal{F}^\dagger(\mathbf{x}_0; \tilde{s}). \quad (9)$$

Optimizing the SL pattern requires solving the inverse projection function \mathcal{F}^\dagger . To generalize this solution, the photometric compensation network (PCNet), is trained to model \mathcal{F}^\dagger using globally matched projector-camera image pairs $(\tilde{\mathbf{x}}; \mathbf{x})$ and corresponding surface images \tilde{s} . PCNet consists of a siamese encoder and a decoder, as shown in Fig. 2. The encoders share weights, and by subtracting the features learned from \tilde{s} from those learned from $\tilde{\mathbf{x}}$, we can separate the varying parts of ambient light, object surface texture, and reflections from the overall photometric model. This allows the network to focus on the photometric effects caused by the projection, giving the photometric compensation network generalization capabilities.

However, many pixels in this process do not conform to physical laws. For instance, if blue light is projected onto an object that absorbs blue light, the surface is expected to appear blue. But adjusting the blue channel values of $\hat{\mathbf{x}}$ using Eq. 9 might not accurately match the effect of \mathbf{x}_0 . Consequently, these pixels may experience brightness and chromaticity clipping, leading to artifacts in the image. To mitigate these artifacts, an additional module was added to the traditional photometric compensation network. This module refines the optimization objective with minimal loss, achieving an optimal solution that meets the intended target.

3.2.2. DeArtifact Module

The DeArtifact module operates after PCNet training is completed, explicitly handling the projection compensation process to minimize artifacts. We use PCNet as the projection module to generate synthetic projection compensation data that better aligns with physical optics. The generated data is then fine-tuned with real data, allowing the DeArtifact module to more accurately identify the pixels needing optimization.

The module identifies and corrects clipping points using three-dimensional TPS interpolation for each pixel. The TPS function is given by Eq. 10.

$$\mathbf{x}^* = f(\mathbf{x}') = \sum_{i=0}^{N-1} \omega_i \phi(\|\mathbf{x}' - \mathbf{x}'_i\|) + \mathbf{a}^T \mathbf{x}' + b, \quad (10)$$

where \mathbf{x}^* is the compensation result, \mathbf{x}' is the captured image, and ω_i , \mathbf{a} , and b are parameters determined by solving

a linear system of equations. To compute the TPS projection compensation function, N sets of projection compensation image pairs are needed. During global matching, a real projection compensation data pair is obtained, while the remaining $N - 1$ simulated pairs are generated using the trained PCNet by swapping input-output pairs. During the parameter computation process, the real data pair $(\mathbf{x}'_{real}, \mathbf{x}^*_{real})$ has a higher weight:

$$\mathbf{w} = (\alpha w_1, \alpha w_2, \dots, (1 - \alpha) w_N)^T \quad \text{where } \alpha = 0.35. \quad (11)$$

To minimize clipping, we need to smoothly adjust the input brightness.

$$\mathbf{x}_{0_{adapt}} = \mathbf{s} * \mathbf{x}_0, \quad (12)$$

First, we define the error functions that will be minimized in the optimization process. The error function includes the saturation error err_{sat} , which prevents color clipping, the gradient variation error err_{grad} , which ensures smooth image adjustments, and the intensity error err_{int} , which maintains overall brightness.

Next, the variable brightness scaling value S is adjusted non-linearly for each pixel. The optimal S is found by minimizing the following objective:

$$S_{opt} = \underset{S}{\operatorname{argmin}} err_{opt}(S). \quad (13)$$

The total error function is:

$$err_{opt}(S) = \omega_{sat} \cdot err_{sat}(S) + \omega_{grad} \cdot err_{grad}(S) + \omega_{int} \cdot err_{int}(S). \quad (14)$$

Here, ω_{sat} , ω_{grad} , and ω_{int} are the weights for each error term.

To mitigate potential inaccuracies in the photometric performance of the TPS function, we introduced a photometric inspector following the optimizer. We also generated uniformly distributed solid-color projection compensation data pairs across the entire color space for testing using PCNet. Since the TPS function computes photometric compensation pixel by pixel, errors in these calculations can lead to color discontinuities. These are detected by calculating the pixel color gradient. However, texture boundaries on the object's surface may inherently result in large gradients. Therefore, image similarity within regions is also considered. Pixels that fail to meet the criteria are excluded from the DeArtifact module via a generated mask, ensuring minimal optimization is applied directly through PCNet.

$$M(p) = \begin{cases} 1 & \text{if } G_p \geq 20 \text{ or } \text{SSIM}(I_{A(p)}, R_{A(p)}) \leq 0.8 \\ 0 & \text{otherwise} \end{cases} \quad (15)$$

Here, G_p represents the color gradient of pixel p , and the SSIM function calculates the image similarity between the region around pixel p with area A and the corresponding reference data region.

4. Experiments

We prepared 40 sets of real data with various settings for PCNet training to enhance the photometric compensation network’s generalization. Twenty sets are from [10], with the remaining 20 sets created by us. We used unwrapped projection compensation data for PCNet training.

Each dataset comprises 700 projection images per object surface, with 500 for training and 200 for testing. During training, we randomly select different object surface images and their corresponding projections to facilitate the separation of global illumination and partial reflections.

In our experiments, we first validate the advantages of our global matching algorithm by comparing it with Gray code mapping and deep learning methods, focusing on continuous global projector-camera mapping. We then demonstrate the optimization effects on common SL patterns, presenting the first unified optimization scheme across different SLs. Decoding accuracy is used to quantify the algorithm’s effectiveness. The equipment used in our experiment includes a Hikvision MV-CU013-A0GC camera (1280x1024) and a Sony VPL-EX570 projector (1024x768).

4.1. Comparison of Global Matching Methods

We first compare our method with traditional Gray code matching. For a fair comparison in obtaining the global projector-camera mapping relationship, we used 42 Gray code SL patterns to encode every pixel on the projector’s image plane. Correspondingly, we only used one SL projection pattern. The results, shown in Fig. 3, indicate that Gray code, despite its global encoding, results in discrete matching due to the lower resolution of the camera’s effective area compared to the projector.

Gray code often produces decoding errors at edges where code values change, leading to periodic black areas and missing matching results. Additionally, on dark textures, Gray code can suffer from code value loss. These issues are reflected in the periodic mismatches and black regions in the matching results, as shown in the fourth column of Fig. 3. In contrast, our proposed method achieves continuous global matching, preserving original texture details.

Next, we compared our method with WarpingNet [12], a deep learning-based method that learns continuous global mapping using 500 projection images. While WarpingNet performs well on continuous surfaces, it struggles with complex surfaces and stacked objects. Our method, which uses only one projection, not only achieves finer and more accurate texture mapping but also provides more detailed results by directly calculating on continuous triangular patches, making it especially effective in complex scenarios.

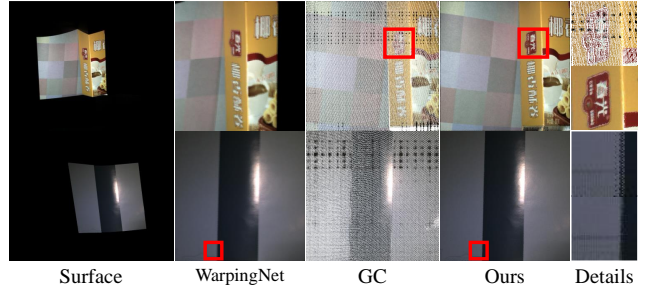


Figure 3. Comparison with the method of global encoding using Gray code (GC) and WarpingNet.

4.2. Optimization Effects of Different Structured Light Patterns

In SL 3D reconstruction, projecting different SL patterns encodes the surface of the object, making decoding accuracy a critical metric for evaluating precision. We tested several common SL patterns on various objects under different lighting conditions. To quantify our algorithm’s optimization effect, we mapped the captured images to the projector’s coordinate system, allowing for a direct comparison of decoding accuracy before and after optimization.

Due to the high generalization capability of our proposed optimization method, we applied different targeted optimization schemes to various SL patterns, demonstrating its superior performance across different scenarios.

4.2.1. Binary Stripe Structured Light Pattern

Gray code encoding is widely used in binary stripe coding. We projected Gray code patterns onto objects under varying lighting conditions and exposures, then decoded the captured images to evaluate decoding accuracy. We compared our method with Fu et al.’s HDR SL optimization [7] and the Exposure Correction (EC) method [40], which post-processes images to correct exposure.

As shown in Fig. 5, the optimization results of different methods are compared. The HDR SL method reduces overexposure by adjusting light intensity but is limited to grayscale optimization. Our method, which optimizes based on object texture, preserves code values and improves accuracy. However, as shown in Fig. 4, the EC method may misinterpret dark textures as underexposure, leading to decoding errors.

These experiments demonstrate the effectiveness of our method in optimizing binary stripe-coded SL patterns.

4.2.2. Speckle Structured Light Pattern

Speckle SL, typically used in sparse matching scenarios, can also suffer from coding errors due to pixel coupling and reflection. We applied HDR SL and EC methods to optimize speckle patterns, as shown in Fig. 5. Although speckle SL has fewer coding patterns and its decoding error rate is

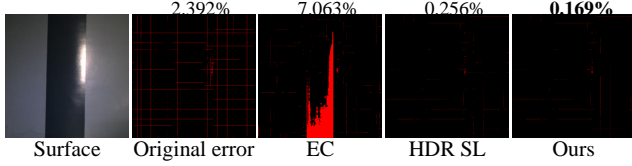


Figure 4. In Scene 3, the EC method incorrectly changes the exposure, leading to a significant increase in the decoding error rate.

higher than that of gray-code patterns, its decoding rules are more robust to grayscale variations. This robustness helps reduce decoding errors caused by incorrect exposure adjustments in the EC method. However, the decoding accuracy of the other two methods is still lower compared to our approach.

We further assessed the optimization performance under varying exposure times and different optimization schemes (Fig. 6). The results demonstrate that extreme exposures reduce decoding accuracy. Within the normal exposure range, all methods showed better optimization performance for lower exposures. Our method, however, consistently ensured higher decoding precision.

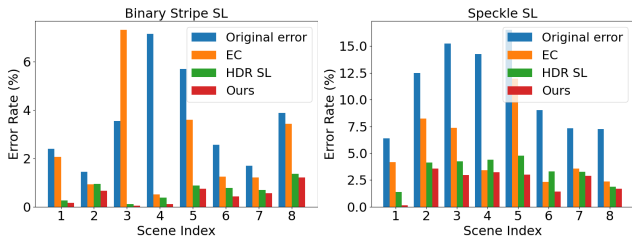


Figure 5. The comparison of the optimized decoding error rates of different methods under various scenes is shown, where the left figure presents the optimization results for binary stripes (Gray code), and the right figure shows the optimization results for speckle structured light.

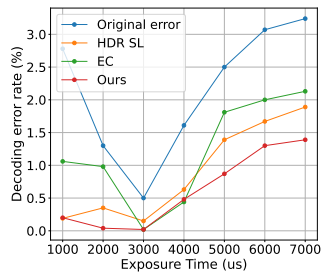


Figure 6. Optimization effect of speckle structured light under different exposures.

4.2.3. Colored Structured Light Pattern

Colored SL encodes information in the color dimension, allowing for higher density encoding with fewer images.

We optimized the classic De Bruijn color stripe pattern and evaluated our results by comparing various optimization methods. Koninckx et al. [16] improves colored SL by calibrating camera and projector response curves, while Dong et al. [6] optimizes without calibration, using a color detection algorithm suitable for the De Bruijn pattern.

For a fair comparison, we pre-calibrated response curves for Koninckx’s method. As shown in Fig. 7, the original decoding accuracy was low, even in non-overexposed areas. Koninckx’s method improves accuracy in extreme exposure regions but struggles in normally exposed areas. Dong’s method improved accuracy, but due to its uniform alteration of the encoding colors, it still results in continuous decoding errors. Our method, with pixel-level optimization, effectively removes artifacts and achieves higher decoding accuracy with fewer continuous errors.

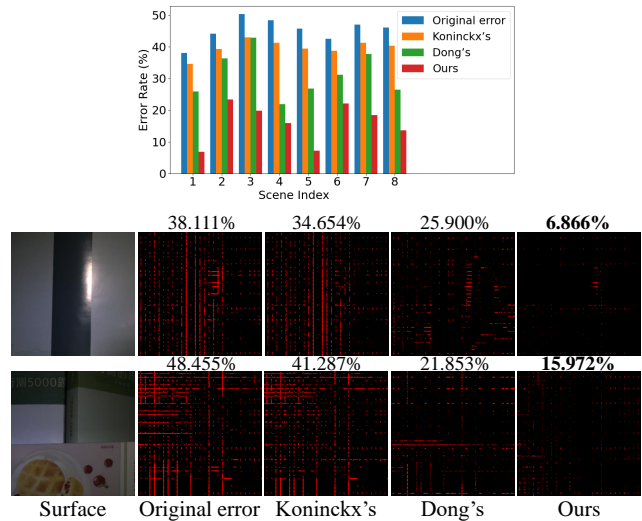


Figure 7. The comparison of the decoding error rates of different methods after optimizing colored structured light under various scenes. The subfigures below show the results for Scene 3 and 4.

5. Ablation Study

5.1. Effect of Global Matching Module

In the Projector-camera global matching module, we employ error code filtering to reduce feature point matching errors during global matching. To demonstrate the effectiveness of this module, we conducted an ablation experiment. After removing the error code filter, we performed triangulation and global mapping on the original matching pairs. The comparative results are shown in the Fig. 8.

When there is continuous loss in the surrounding De Bruijn encoding, the orange-red dots may experience decoding errors, leading to incorrect placement. This can result in erroneous triangle color mapping, as shown in the

figure. After filtering out these errors, the region is correctly matched through re-triangulation and color mapping within the triangles.

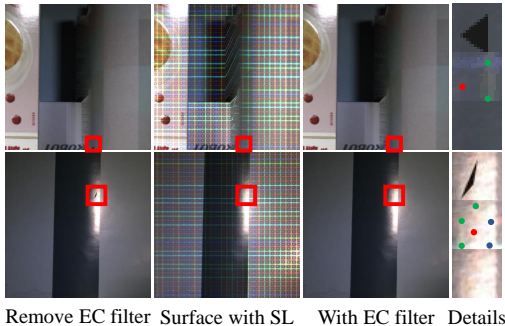


Figure 8. Global matching results with and without the error code (EC) filter. The fourth column is an enlarged view of the erroneous matches, with red dots indicating incorrect matches, green dots indicating correct matches, and blue dots indicating unmatched points.

5.2. Effect of DeArtifact Module

In SL projection optimization, we propose the DeArtifact module to reduce artifacts that traditional projection compensation networks cannot avoid. We first use the pre-trained PCNet as the projection network to provide the TPS function with foundational training data, ensuring its accuracy. Then, we incorporate a SL image pair as real data into the TPS function training, adjusting data weights to achieve a photometric model closer to reality. To demonstrate the contributions of the projection network and real data, we conducted ablation experiments comparing the accuracy of the resulting TPS photometric models.

If we do not use the training data generated by the projection network, we simulate the projection process using a multiplication blend (MB) mode, processed by PCNet to obtain photometric compensation images for TPS training. We compare the effects of including or excluding a real SL data pair during training to assess its impact on improving the photometric model.

As shown in Fig. 9, results indicate that without the projection network, the TPS function can lead to significant color deviations or data loss. Incorporating real SL data improves accuracy but still shows deviations. Using projection network data brings the TPS function’s photometric expression closer to reality, and adding a SL data pair allows for fine-tuning that more closely matches the ground truth.

To evaluate the impact of different methods on the TPS function’s ability to reduce artifacts, we compared their effectiveness in artifact optimization using image quality metrics such as SSIM, PSNR, and RMSE. SSIM measures the structural similarity between the optimized image and the original, highlighting perceptual differences in texture and

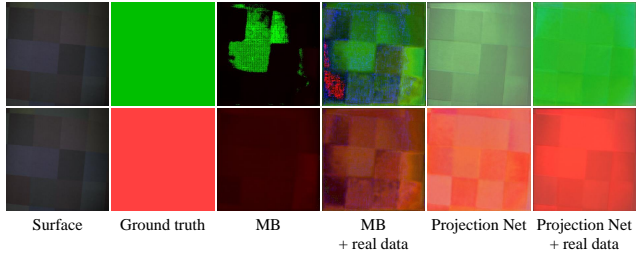


Figure 9. The photometric results of the TPS function.

shape. PSNR quantifies the peak signal-to-noise ratio, indicating the level of distortion between the images. RMSE evaluates the root mean square error, providing a numerical measure of the differences in pixel intensity. In the DeArtifact module’s optimizer, the TPS function’s photometric expression is first checked. Pixels that cannot accurately express photometric information are excluded from artifact optimization. As a result, the ablation study shows that an inaccurate TPS function does not negatively impact the projection optimization process (Table 1).

Table 1. The comparison between the optimized projection results and the projection inputs.

	SSIM \uparrow	PSNR \uparrow	RMSE \downarrow
Without DeArtifact module	0.745	19.055	28.482
Multiply blend	0.745	19.079	28.352
Multiply blend + real data	0.759	19.585	26.746
Projection Net	0.831	21.041	22.619
Projection Net + real data	0.858	22.722	18.638

In our experiment, the SL projection input to be optimized is a colored grid (Fig. 1), a common type of SL that uses unique color coding to determine the projection position. We tested our method on a self-captured dataset, and the experimental results, as shown in Table 1, indicate that our proposed method achieves smoother and more natural transitions in regions with color changes and significantly improves color fidelity. The image quality metrics calculated between the different optimized results and the original input images quantitatively demonstrate the optimization effects of each module in DeArtifact.

6. Conclusion

In this paper, we propose a unified framework for structured light pattern optimization. It requires only a single projection to quickly achieve targeted projection optimization for various scenes and any type of structured light. Through comprehensive experiments, we evaluated the optimization effects of three common types of structured light and demonstrated that our method outperforms state-of-the-art techniques both qualitatively and quantitatively. Additionally, ablation studies confirm the reliabil-

ity of our projector-camera matching and artifact removal strategies.

References

- [1] David Bak. Rapid prototyping or rapid production? 3d printing processes move industry towards the latter. *Assembly Automation*, 2003. 1
- [2] Nicholas James Beresford Brereton, Farah Ahmed, Daniel Sykes, Michael Jason Ray, Ian Shield, Angela Karp, and Richard James Murphy. X-ray micro-computed tomography in willow reveals tissue patterning of reaction wood and delay in programmed cell death. *BMC plant biology*, 15:1–12, 2015. 1
- [3] Jen A Bright, Jesús Marugán-Lobón, Emily J Rayfield, and Samuel N Cobb. The multifactorial nature of beak and skull shape evolution in parrots and cockatoos (psittaciformes). *BMC Evolutionary Biology*, 19:1–9, 2019. 1
- [4] Elisabetta Cilli, Francesco Fontani, Marta Maria Ciucani, Marcella Pizzuto, Pierangelo Di Benedetto, Sara De Fanti, Thomas Mignani, Carla Bini, Rocco Iacovera, Susi Pelotti, et al. Museomics provides insights into conservation and education: The instance of an african lion specimen from the museum of zoology “pietro doederlein”. *Diversity*, 15(1):87, 2023. 1
- [5] Andrea D’Eusanio, Stefano Pini, Guido Borghi, Roberto Vezzani, and Rita Cucchiara. Refinet: 3d human pose refinement with depth maps. In *2020 25th International Conference on Pattern Recognition (ICPR)*, pages 2320–2327. IEEE, 2021. 1
- [6] Xin Dong, Haibin Ling, and Bingyao Huang. Adaptive color structured light for calibration and shape reconstruction. In *IEEE International Symposium on Mixed and Augmented Reality (ISMAR)*, pages 1240–1249. IEEE, 2023. 3, 7
- [7] Yichen Fu, Junfeng Fan, Fengshui Jing, and Min Tan. High dynamic range structured light 3-d measurement based on region adaptive fringe brightness. *IEEE Transactions on Industrial Electronics*, 2023. 6
- [8] Kensaku Fujii, Michael D Grossberg, and Shree K Nayar. A projector-camera system with real-time photometric adaptation for dynamic environments. In *IEEE Conference on Computer Vision and Pattern Recognition (CVPR)*, pages 814–821. IEEE, 2005. 2
- [9] Pratibha Gupta. *Gray code composite pattern structured light illumination*. PhD thesis, University of Kentucky Libraries, 2007. 2
- [10] Bingyao Huang and Haibin Ling. End-to-end projector photometric compensation. In *IEEE Conference on Computer Vision and Pattern Recognition (CVPR)*, pages 6810–6819, 2019. 6
- [11] Bingyao Huang, Samed Ozdemir, Ying Tang, Chunyuan Liao, and Haibin Ling. A single-shot-per-pose camera-projector calibration system for imperfect planar targets. In *2018 IEEE International Symposium on Mixed and Augmented Reality Adjunct (ISMAR-Adjunct)*, pages 15–20. IEEE, 2018. 2
- [12] Bingyao Huang, Tao Sun, and Haibin Ling. End-to-end full projector compensation. *IEEE Transactions on Pattern Analysis and Machine Intelligence*, 44(6):2953–2967, 2021. 2, 6
- [13] Tong Jia, Xiaofang Li, Xiao Yang, Shuyang Lin, Yizhe Liu, and Dongyue Chen. Adaptivestereo: Depth estimation from adaptive structured light. *Optics & Laser Technology*, 169: 110076, 2024. 3
- [14] Achuta Kadambi, Ayush Bhandari, and Ramesh Raskar. 3d depth cameras in vision: Benefits and limitations of the hardware: With an emphasis on the first- and second-generation kinect models. *Computer vision and machine learning with RGB-D sensors*, pages 3–26, 2014. 1
- [15] Hiroshi Kawasaki, Ryo Furukawa, Ryusuke Sagawa, and Yasushi Yagi. Dynamic scene shape reconstruction using a single structured light pattern. In *IEEE Conference on Computer Vision and Pattern Recognition (CVPR)*, pages 1–8. IEEE, 2008. 4
- [16] Thomas P Koninckx, Pieter Peers, Philip Dutré, and Luc Van Gool. Scene-adapted structured light. In *IEEE Conference on Computer Vision and Pattern Recognition (CVPR)*, pages 611–618. IEEE, 2005. 7
- [17] Hiroki Kusuyama, Yuta Kageyama, Daisuke Iwai, and Kosuke Sato. A multi-aperture coaxial projector balancing shadow suppression and deblurring. *IEEE Transactions on Visualization and Computer Graphics*, 2024. 2
- [18] Marion Leménager, Jérôme Burkiewicz, Daniel J Schoen, and Simon Joly. Studying flowers in 3d using photogrammetry. *New Phytologist*, 237(5):1922–1933, 2023. 1
- [19] Yuqi Li, Wenting Yin, Jiabao Li, and Xijiong Xie. Physics-based efficient full projector compensation using only natural images. *IEEE Transactions on Visualization and Computer Graphics*, 2023. 2
- [20] Joshua J Medina, James M Maley, Siddharth Sannapareddy, Noah N Medina, Cyril M Gilman, and John E McCormack. A rapid and cost-effective pipeline for digitization of museum specimens with 3d photogrammetry. *Plos one*, 15(8): e0236417, 2020. 1
- [21] Gaku Narita, Yoshihiro Watanabe, and Masatoshi Ishikawa. Dynamic projection mapping onto deforming non-rigid surface using deformable dot cluster marker. *IEEE Transactions on Visualization and Computer Graphics*, 23(3):1235–1248, 2016. 2
- [22] Chuong V Nguyen, David R Lovell, Matt Adcock, and John La Salle. Capturing natural-colour 3d models of insects for species discovery and diagnostics. *PloS one*, 9(4):e94346, 2014. 1
- [23] J. Pages, J. Salvi, R. Garcia, and C. Matabosch. Overview of coded light projection techniques for automatic 3d profiling. In *IEEE International Conference on Robotics and Automation*, pages 133–138 vol.1, 2003. 2
- [24] Jino Park, Donghyuk Jung, and Bochang Moon. Projector compensation framework using differentiable rendering. *IEEE Access*, 10:44461–44470, 2022. 2
- [25] Martin Postma, Adrian Stephen Wolferstan Tordiffe, MS Hofmeyr, Ryan Rudolf Reisinger, L Catherine Bester, Peter Erik Buss, and PJN De Bruyn. Terrestrial mammal three-dimensional photogrammetry: multispecies mass estimation. *Ecosphere*, 6(12):1–16, 2015. 1

- [26] Jiaming Qian, Shijie Feng, Tianyang Tao, Yan Hu, Kai Liu, Shuaijie Wu, Qian Chen, and Chao Zuo. High-resolution real-time 360° 3d model reconstruction of a handheld object with fringe projection profilometry. *Optics letters*, 44(23): 5751–5754, 2019. 1
- [27] Jiaming Qian, Shijie Feng, Mingzhu Xu, Tianyang Tao, Yuhao Shang, Qian Chen, and Chao Zuo. High-resolution real-time 360° 3d surface defect inspection with fringe projection profilometry. *Optics and Lasers in Engineering*, 137: 106382, 2021. 1
- [28] Ramesh Raskar, Jeroen van Baar, and Jin Xiang Chai. A low-cost projector mosaic with fast registration. In *Asian Conference on Computer Vision (ACCV)*, 2002. 2
- [29] Paula Redweik, Susana Reis, and Maria Cristina Duarte. A digital botanical garden: Using interactive 3d models for visitor experience enhancement and collection management. *Virtual Archaeology Review*, 14(28):65–80, 2023. 1
- [30] Miguel Ribo and Markus Brandner. State of the art on vision-based structured light systems for 3d measurements. In *International Workshop on Robotic Sensors: Robotic and Sensor Environments*, pages 2–6. IEEE, 2005. 1
- [31] Joan R Rosell-Polo, Fernando Auat Cheein, Eduard Gregorio, Dionisio Andújar, Lluís Puigdomènech, Joan Masip, and Alexandre Escolà. Advances in structured light sensors applications in precision agriculture and livestock farming. *Advances in agronomy*, 133:71–112, 2015. 1
- [32] Alice Ruget, Max Tyler, Germán Mora Martín, Stirling Scholes, Feng Zhu, Istvan Gyongy, Brent Hearn, Steve McLaughlin, Abderrahim Halimi, and Jonathan Leach. Pixels2pose: Super-resolution time-of-flight imaging for 3d pose estimation. *Science Advances*, 8(48):eade0123, 2022. 1
- [33] Giovanna Sansoni, Marco Trebeschi, and Franco Docchio. State-of-the-art and applications of 3d imaging sensors in industry, cultural heritage, medicine, and criminal investigation. *Sensors*, 9(1):568–601, 2009. 1
- [34] Kuang-Tsu Shih, Jen-Shuo Liu, Frank Shyu, and Homer H Chen. Enhancement and speedup of photometric compensation for projectors by reducing inter-pixel coupling and calibration patterns. *IEEE Transactions on Image Processing*, 30:418–430, 2020. 2
- [35] Jamie Shotton, Andrew Fitzgibbon, Mat Cook, Toby Sharp, Mark Finocchio, Richard Moore, Alex Kipman, and Andrew Blake. Real-time human pose recognition in parts from single depth images. In *CVPR 2011*, pages 1297–1304. IEEE, 2011. 1
- [36] Masatoki Sugimoto, Daisuke Iwai, Koki Ishida, Parinya Punpongsonon, and Kosuke Sato. Directionally decomposing structured light for projector calibration. *IEEE Transactions on Visualization and Computer Graphics*, 27(11): 4161–4170, 2021. 2
- [37] Alex Turpin, Gabriella Musarra, Valentin Kapitany, Francesco Tonolini, Ashley Lyons, Ilya Starshynov, Federica Villa, Enrico Conca, Francesco Fioranelli, Roderick Murray-Smith, et al. Spatial images from temporal data. *Optica*, 7(8):900–905, 2020. 1
- [38] Ho Lam Wang, Tin Hang Wong, Yiu Man Chan, Yat Sum Cheng, and David Tai Wai Lau. Photogrammetric reconstruction of 3d carpological collection in high resolution for plants authentication and species discovery. *Plos one*, 17(8): e0270199, 2022. 1
- [39] Xianmin Xu, Yuxin Lin, Haoyang Zhou, Chong Zeng, Yaxin Yu, Kun Zhou, and Hongzhi Wu. A unified spatial-angular structured light for single-view acquisition of shape and reflectance. In *IEEE Conference on Computer Vision and Pattern Recognition (CVPR)*, pages 206–215, 2023. 2
- [40] Zhen Zou, Wei Yu, Jie Huang, and Feng Zhao. Semantic pre-supplement for exposure correction. In *IEEE Conference on Computer Vision and Pattern Recognition Workshops (CVPRW)*, pages 5961–5970, 2024. 6